1 CE-DYNAM (v1), a spatially explicit, process-based carbon erosion

2 scheme for the use in Earth system models

3 Victoria Naipal[1], Ronny Lauerwald[2], Philippe Ciais[1], Bertrand Guenet[1], Yilong Wang[1]

4 [1]Laboratoire des Sciences des Sciences du Climat et de l'Environnement, CEA CNRS UVSQ, Gif-sur-Yvette 91191,

5 France

6 [2]Department of Geoscience, Environment and Society, Université Libre de Bruxelles, Brussels, Belgium

8 *Correspondence :* Victoria Naipal (vnaipal24@gmail.com)

10 **Abstract.**

12 Soil erosion by rainfall and runoff is an important process behind the redistribution of soil organic carbon (SOC) over land,

13 hereby impacting the exchange of carbon (C) between land, atmosphere and rivers. However, the net role of soil erosion in

14 the global C cycle is still unclear as it involves small-scale SOC removal, transport and re-deposition processes that can

15 only be addressed over selected small regions with measurements and models. This leads to uncertainties in future

16 projections of SOC stocks and complicates the evaluation of strategies to mitigate climate change through increased SOC

17 sequestration.

19 In this study we present the parsimonious process-based Carbon Erosion DYNAMics model (CE-DYNAM) that links

20 sediment dynamics resulting from water erosion with the C cycle along a cascade of hillslopes, floodplains and rivers. The

21 model simulates horizontal soil and C transfers triggered by erosion across landscapes and the resulting changes in land-

22 atmosphere CO_2 fluxes at a resolution of about 8 km at the catchment scale. CE-DYNAM is the result of the coupling of a

23 previously developed coarse-resolution sediment budget model and the ecosystem C cycle and erosion removal model

24 derived from the ORCHIDEE land surface model. CE-DYNAM is driven by spatially explicit historical land use change,

25 climate forcing, and global atmospheric CO_2 concentrations affecting ecosystem productivity, erosion rates and residence

26 times of sediment and C in deposition sites. The main features of CE-DYNAM are (1) the spatially explicit simulation of

27 sediment and C fluxes linking hillslopes and floodplains, (2) the low number of parameters that allow running the model at

28 large spatial scales and over long-time scales, and (3) its compatibility with any global land surface model, hereby,

29 providing opportunities to study the effect of soil erosion under global changes.

31 We present the model structure, concepts, and evaluation at the scale of the Rhine catchment for the period 1850-2005 AD.

32 Model results are validated against independent estimates of gross and net soil and C erosion rates, and the spatial

33 variability of SOC stocks from high-resolution modeling studies and observational datasets. We show that despite local

34 differences, the resulting soil and C erosion rates, and SOC stocks from our rather coarse-resolution modelling approach

35 are comparable to high-resolution estimates and observations at sub-basin level. The model also shows that SOC storage

36 increases exponentially with basin area for floodplains in contrast to hillslopes as is seen in observations. We find that soil

37 erosion mobilized 159 Tg (10^{12} g) of C under changing climate and land use, assuming that the erosion loop of the C cycle

38 was in near steady-state by 1850. This caused a net C sink equal to 1% of the Net Primary Productivity of the Rhine

39 catchment over 1850-2005 AD. This sink is a result of the dynamic replacement of C on eroding sites that increases in this

40 period due to rising atmospheric CO_2 concentrations enhancing the litter C input to the soil from primary production.

41

42 **Keywords:** soil erosion; regional carbon cycle; carbon sink; Rhine catchment

43

44 **1 Introduction**

45

46 Soils contain more carbon (C) than the atmosphere and living biomass together. Relatively small disturbances

47 (anthropogenic or natural) to soil C pools over large areas could add up to substantial C emissions (Ciais et al., 2013). With

48 the removal of natural vegetation and the introduction of mechanized agriculture, humans have accelerated soil erosion

49 rates. Over the last two to three decades, studies have shown that water erosion (soil erosion by rainfall and runoff)

50 amplified by human activities has substantially impacted the terrestrial C budget (Doetterl et al., 2012; Lal, 2003; Lugato et

51 al., 2018; Van Oost et al., 2007, 2012; Stallard, 1998; Wang et al., 2017). However, the net effect of water erosion on the C

52 cycle at regional to global scale is still under debate. This leads to uncertainties in the future projections of the soil organic

53 C (SOC) reservoir, and complicates the evaluation of strategies to mitigate climate change by increased SOC sequestration.

54 The study of Stallard (1998) was one of the first to show that water erosion does not only lead to additional C emissions

55 but can also sequester C due to the photosynthetic replacement of SOC at eroding sites and the stabilization of SOC in

56 deeper layers at burial sites. The study of van Oost et al. (2007) was the first to confirm the importance of the sequestration

57 of SOC by agricultural erosion at global scale using isotope tracers. Wang et al. (2017) gathered data on SOC profiles from

58 erosion and deposition sites and confirmed that water erosion on agricultural land that started from the early/middle

59 Holocene has caused a large net global land C sink. Other studies, however, argue that soil erosion is a net C source to the

60 atmosphere due to increased SOC decomposition following soil aggregate breakdown during transport and at deposition

61 sites (Lal et al, 2003; Lugato et al., 2018). Most studies modeling soil erosion and its net effect on SOC dynamics at global

62 scale, however, did not account for the full range of complex effects of climate change, CO_2 fertilization increasing

63 productivity and potentially soil C inputs, harvest of biomass, land use change, and changes in cropland management. In

64 addition, models used at large spatial scales mainly focus on hillslopes and removal processes and neglect floodplain

65 sediment and SOC dynamics. This can lead to substantial biases in the assessment of net effects of SOC erosion at

66 catchment scale because floodplains can store substantial amounts of sediment and C (Berhe et al., 2007; Hoffmann et al.,

67 2013a).

68

69 Furthermore, soil erosion is one of the main contributors to particulate organic carbon (POC) fluxes in rivers and C export

70 to the coastal ocean. The riverine POC fluxes are usually much smaller than the SOC erosion fluxes, because only a small

71 fraction of eroded material is entering the river network and POC losses in the river network occur due to decomposition

72 and burial on floodplains and in benthic sediments. Therefore, uncertainties in large-scale SOC erosion rates will lead to

73 even larger uncertainties in lateral C fluxes between land and ocean for past and future scenarios estimated by global

74 empirical models on riverine C export (Ludwig and Probst, 1998; Mayorga et al., 2010).

75

76 To address these knowledge gaps, we present a parsimonious process-based modelling approach that integrates sediment

77 dynamics resulting from water erosion with SOC dynamics and the horizontal transport of sediment and C in the

78 continuum from hillslopes, to floodplains and rivers. With this approach we are not only able to simulate lateral soil and C

79 transfers triggered by erosion across landscapes but also the resulting changes in the land-atmosphere CO_2 fluxes. The

80 modelling approach uses a simple sediment budget model which is coupled to SOC erosion removal, C input from litter

81 fall, and SOC decomposition processes diagnosed from the ORCHIDEE global land surface model (LSM) in an offline

82 setting (Naipal et al., 2018). We parameterized and applied the resulting model, known as CE-DYNAM for the Rhine

83 catchment, although it is intended to be made applicable to other large catchments globally. CE-DYNAM combines soil

84 erosion processes, for which small scale differences in topography are of utter importance, with a state-of-the-art

85 representation of large-scale SOC dynamics driven by land use and environmental factors (climate, atmospheric CO_2) as

86 simulated by the ORCHIDEE LSM. The flexible structure of CE-DYNAM makes the model adaptable to the SOC

87 dynamics of any other LSM. In this way it is possible to study the main processes behind the linkages between soil erosion

88 and the global C cycle.

89

90 In the next sections we give a detailed overview of CE-DYNAM model structure, the coupling of erosion, deposition and

91 transport with the coarse-resolution SOC dynamics of ORCHIDEE. We then discuss its application for the Rhine

92 catchment, model limitations, uncertainties and its potentials.

93

94 **2 Methods**

95

96 **2.1 General model description**

97

98 CE-DYNAM version 1 (v1) is the result of coupling a large-scale erosion and sediment budget model (Naipal et al., 2016)

99 with the SOC scheme of the land surface model ORCHIDEE (Krinner et al., 2005). The most important features of the

100 model are (1) the spatially explicit simulation of lateral sediment and C transport fluxes linking hillslopes and floodplains,

101 (2) consistent simulation of vertical C fluxes coupled with horizontal transport, (3) the low number of parameters that

102 allows running the model at large spatial scales and over long time-scales up to several thousands of years, (4) generic

103 input fields for application to any region or catchment, and (5) compatibility with land surface models (LSMs).

104

105 In the ORCHIDEE LSM, terrestrial C is represented by 8 biomass pools, 4 litter pools and 3 SOC pools. Each of the pools

106 varies in space, time and over the 12 Plant Functional Types (PFTs). An extra PFT is used to represent bare soil. Natural

107 and anthropogenic disturbances to the C pools include fire, crop harvest, changes to GPP, litterfall, autotrophic and

108 heterotrophic respiration as a result of climatic changes (Krinner et al., 2005; Guimberteau et al., 2018). The C-cycle

109 processes are represented by a C emulator that reproduces for each PFT all C pools and fluxes between the pools exactly as

110   in ORCHIDEE in absence of erosion. A net land use change scheme is included in the emulator with mass-conservative

111   bookkeeping of SOC and C input when a PFT is changed into another from anthropogenic land use change (Naipal et al.,

112   2018). The sediment budget model has been added in the emulator to simulate large-scale long-term soil and SOC

113   redistribution by water erosion using coarse-resolution precipitation, land-cover and LAI data from Earth System Models

114   (Naipal et al. 2015, 2016). The C emulator including erosion removal was developed by Naipal et al. (2018) to reproduce

115   SOC vertical profile, removal of soil and SOC starting from the topsoil, and compensatory SOC storage from litter input.

116   As soil erosion is assumed not to change soil and hydraulic parameters but only the SOC dynamics, the emulator allows

117   substituting for the ORCHIDEE model and performing simulations on time scales of millennia with a daily time step,

118   which would be a very computationally expensive or nearly impossible with the full LSM. The concept and all equations of

119   the emulator are described in Naipal et al. (2018). The following subsections describe the different components of the CE-

120   DYNAM that couples the C and soil removal scheme (Naipal et al., 2018) with the horizontal transport and burial of

121   eroded soil and C (Naipal et al., 2016).

122

2.2 The soil erosion scheme

124

The potential gross soil erosion rates are calculated by the Adjusted Revised Universal Soil Loss Equation (Adj. RUSLE)

126   model (Naipal et al., 2015), which is part of the sediment budget model (Fig 1). In the Adj. RUSLE the yearly average soil

127   erosion rate is a product of rainfall erosivity (R), slope steepness (S), land cover and management (Cm) and soil erodibility

128   (K):

129

130    $$E = S * R * K * Cm \tag{1}$$

131

The slope-length (L) and support practice (P) factors, which are part of the original Revised Universal Soil Loss Equation

133   (RUSLE) model (Renard et al., 1997), have been excluded here because their quantification still includes many

134   uncertainties and is not practical for applications at regional to global scales. These factors are a function of local manmade

135   structures and management practices which are difficult to assess for present day and whose changes over the past are even

136   more uncertain. In addition, we focus in this study on potential soil erosion and do not consider erosion-control practices.

137   Naipal et al. (2015) have developed a methodology to derive the slope factor S and the erosivity factor R from 5 arcmin

138   resolution data on elevation and precipitation, hereby preserving the high-resolution spatial variability in slope and

139   temporal variability in erosivity. Despite the comparatively coarse resolution of the erosion model, the so derived R factor

140   was shown to compare well with the corresponding high-resolution product published by Panagos et al. (2017).

141

2.3 The sediment deposition and transport scheme

143

The sediment deposition and transport scheme have been adapted from the sediment budget model described by Naipal et

145   al. (2016), which has been calibrated and validated for the Rhine catchment (Fig 1). In the sediment budget model each

146   grid cell contains a floodplain fraction, which is needed to ensure sediment transport between the grid cells (transport from

147   one grid cell to another can only follow the connectivity of floodplains). We followed a 2-step methodology to derive

148   floodplains in the Rhine catchment, as soil databases usually do not identify floodplain soil as a separate soil class. First,

149   grid cells were identified that consisted entirely out of floodplains. For this we used the gridded global data set of soil at 5

150   arcminute resolution, with intact regolith, and sedimentary deposit thicknesses of Pelletier et al. (2016) (Table 1), and

151   identified lowlands and hillslopes based on soil thickness and depth to bedrock. The lowlands were classified as grid cells

152   that contain only floodplains and no hillslopes. Second, we calculated the floodplain fraction of a grid cell (A_{fl}) that has

153   both hillslopes and floodplains as a function of stream length and width based on the methodology developed by Hoffmann

154   et al. (2007):

156    $$A_{fl} = L_{stream} * W_{stream} \tag{2}$$

158   where L_{stream} is the stream length derived from the HydroSHEDS database (Lehner and Grill, 2013) (Table 1).

160    $$W_{stream} = a * A_{upstream}^{b} \tag{3}$$

162   Where, $A_{upstream}$ is the upstream catchment area, and a is equal to 60.8, and b is equal to 0.3.

164   The parameters a and b have been derived from the scaling behavior of floodplain width as estimated from measurements

165   on the Rhine (Hoffmann et al., 2007). The sediment deposition on hillslopes (D_{hs}) and floodplains (D_{fl}) is calculated as a

166   function of the gross soil removal rates (E) with the following equations:

168    $$D_{fl} = f * E \tag{4a}$$

169    $$D_{hs} = (1 - f) * E \tag{4b}$$

170    $$f = a_f * e^{\left(\frac{b_f * \theta}{\theta_{max}}\right)} \tag{5}$$

172   Where, f is the floodplain deposition factor at 8 km resolution that determines the fraction of gross eroded material

173   transported and deposited in the floodplain fraction of a grid cell. a_f and b_f are constant parameters that relate f to the

174   average topographical slope (θ) of a grid cell depending on the type of land cover . θ_{max} us the maximum topographical

175   slope of the entire Rhine catchment.

177   The parameters a_f and b_f are chosen in such a way that f varies between 0.2 and 0.5 for cropland, reflecting the decreased

178   sediment connectivity between hillslopes and floodplains created by manmade structures such as ditches and hedges. For

179   natural vegetation such as forest and natural grassland, a_f and b_f are chosen in a way that f varies between 0.5 and 0.8

180   assuming that in these landscapes hillslopes and floodplains are well-connected. In each case and within the defined

181   boundaries, the slope gradient determines the final value of f. Eroded material that has not been deposited in the floodplains

182   stays on the hillslopes and is assumed to be deposited at the foot of the hillslopes as colluvial sediment.

183

184 The floodplain fractions of the grid cells are connected through a 8 km resolution flow routing network (Naipal et al.,
185 2016), where the rivers and streams are indirectly included in the floodplain area but not explicitly simulated. By routing
186 the sediment and C through the floodplain fractions of grid cells we lump together the slow process of riverbank erosion by
187 river dynamics (time scale ≈ a few years to thousands of years), and the rather fast process of transport of eroded material
188 by the rivers (time scale ≈ days). The rate by which sediment and SOC leave the floodplain of a grid cell to go to the
189 floodplain of an adjacent grid cell is determined by the sediment residence time. The sediment residence time (τ) is a
190 function of the upstream contributing area (*Flowacc*):

191

192 $$\tau = e^{\frac{Flowacc - a_\tau}{b_\tau}}$$ (6)

193

194 The study of Hoffmann et al. (2008) shows that the majority of floodplain sediments have a residence time that ranges
195 between 0 and 2000 years, with a median of 50 years. The constants a_τ and b_τ are chosen in such way that basin τ varies
196 between the 5th and 95th percentile of those observations, with a median for the whole catchment of 50 years. These
197 constants are uniform for the whole basin. Floodplain C storage follows the same residence time as sediment on top of the
198 actual decomposition rate of C in a grid cell of ORCHIDEE. The routing of sediment and C between the grid cells follows
199 a multiple-flow routing scheme. In this scheme the flow coming from a certain grid cell is distributed across all lower-lying
200 neighbors based on a weight (*W*, dimensionless) that is calculated as a function of the contour length (*c*):

201

202 $$W_{(i+k,j+l)} = \frac{\theta_{(i+k,j+l)} * c_{(i+k,j+l)}}{\sum_{k,l=-1}^{k,l=1} \left[\theta_{(i+k,j+l)} * c_{(i+k,j+l)} \right]}$$ (7)

203

204 Where *c* is 0.5*grid size (m) in the cardinal direction and 0.354* grid size (m) in the diagonal direction. (*i, j*) is the grid cell
205 in consideration where *i* counts grid cells in the latitude direction and *j* in the longitude direction. *i+k* and *j+l* specify the
206 neighboring grid cell where k and l can be either -1, 0 or 1. θ is calculated as the division between the difference in
207 elevation (*h*) give in meters difference and the grid cell size (*d*), also in meters:

208

209 $$\theta_{(i+k,j+l)} = \frac{h_{(i,j)} - h_{(i+k,j+l)}}{d}$$ (8)

210

211 The sediment and C routing is done continuously at a daily time-step to preserve numerical stability of the model. More
212 detailed explanation of the methods presented in this section can be found in the study of Naipal et al. (2016).

213

214 **2.4 Litter dynamics**

215

216 The four litter pools in the emulator are an below- and an above- ground litter pool, each split into a metabolic and a
217 structural pool with different turnover rates as implemented in ORCHIDEE (Krinner et al., 2005). The belowground litter
218 pools consist mostly out of root residues. Both the biomass and litter pools have a loss flux due to fire as incorporated in
219 ORCHIDEE by the Spitfire model of Thonicke et al. (2010). The litter that is not respired or burnt is transferred to the SOC

220   pools based on the Century model (Parton et al., 1987) and the vertical discretization scheme SOC scheme presented by
221   Naipal et al., (2018).

222

223   The vertical discretization scheme was introduced in the emulator to account for a declining C input and SOC respiration
224   with depth, and consists of 20 layers with each 10 cm thickness. The litter to soil fluxes from above-ground litter pools are
225   all attributed to the top 10 cm of the soil profile. The litter to soil fluxes from belowground litter pools are distributed
226   exponentially over the whole soil profile according to:

227

228    $I_{be}(z) = I_{0be} * e^{-r*z}$ (9)

229

230   Where I_{0be} is the below-ground litter input to the surface soil layer and r is the PFT-specific vertical root-density
231   attenuation coefficient as used in ORCHIDEE. The sum of all layer-dependent litter to soil fractions is equal to the total
232   litter to soil flux as calculated by ORCHIDEE. The vertical SOC profile is modified by erosion and the resulting deposition
233   fluxes, which is discussed in detail the following sections.

234

2.5 Crop harvest and yield

236

237   We adjusted the representation of crop harvest from ORCHIDEE by assuming a variable harvest index for C3 plants that
238   increases during the historical period as shown in the study of Hay (1995) for Wheat and Barley, which are also the main
239   C3 crops in the Rhine catchment. The harvest index is defined by the ratio of harvested grain biomass to above-ground dry
240   matter production (Krinner et al., 2005). In this study the harvest index increases linearly between 0.26 and 0.46 (Naipal et
241   al. 2018) consistent with the average values of Hay (1995). We also found that in certain cases the cropland NPP was too
242   high during the entire period of 1850-2005, especially in the early part of the 20th Century. This is because the cropland
243   photosynthetic rates were adjusted in ORCHIDEE to give a cropland NPP representative of present day values that are
244   higher than for the low input agriculture of the early 20th Century. To derive a more realistic NPP for crop and barley in the
245   Rhine catchment we used the long-term crop yield data obtained from a dataset on 120000 yield observations over the 20th
246   century in Northeast French Départements (NUTS3 administrative division) (Schauberger et al., 2018). According to the
247   yield data assembled by Schauberger et al. (2018), yields in Northeast France for these crops increased fourfold during the
248   last century. Note that crop residues like straw constituted a larger fraction of the total biomass in 1850 than in 2005, but
249   those residues were likely collected and used for animal feed, housing fuel. We did not account for this harvest of residue
250   in the simulation of SOC.

251

2.6 SOC dynamics without erosion

253

254   The change in the carbon content of the PFT-specific SOC pools in the emulator without soil erosion as described by
255   Naipal et al. (2018) (Fig 1):

256

257 $$\frac{dSOC_a(t)}{dt} = lit_a(t) + k_{pa} * SOC_p(t) + k_{sa} * SOC_s(t) - (k_{ap} + k_{as} + k0_a) * SOC_a(t)$$ (10)

258 $$\frac{dSOC_s(t)}{dt} = lit_s(t) + k_{as} * SOC_a(t) - (k_{sa} + k_{sp} + k0_s) * SOC_a(t)$$ (11)

259 $$\frac{dSOC_p(t)}{dt} = k_{ap} * SOC_a(t) + k_{sp} * SOC_s(t) - (k_{pa} + k0_p) * SOC_p(t)$$ (12)

260

261 Where, SOC_a, SOC_s, and SOC_p (g C m^{-2}) are the active, slow and passive SOC, respectively. The distinction of these SOC

262 pools, defined by their residence times, are based on the study of Parton *et al.* (1987). The active SOC pool has the lowest

263 residence time (1 - 5 years) and the passive the highest (200-1500 years). lit_a and lit_s (g C m^{-2} day^{-1}) are the daily litter

264 input rates to the active and slow SOC pools, respectively; $k0_a$, $k0_s$ and $k0_p$ (day^{-1}) are the respiration rates of the active,

265 slow and passive pools, respectively; k_{as}, k_{ap} , k_{pa}, k_{sa}, k_{sp} are the coefficients determining the flux from the active to the

266 slow pool, from the active to the passive pool, from the passive to the active pool, from the slow to the active pool and

267 from the slow to the passive pool, respectively.

268 The vertical C discretization scheme in the emulator assumes that the SOC respiration rates decrease exponentially with

269 depth:

270

271 $$k_i(z) = k_{0i}(z) * e^{-re*z}$$ (13)

272

273 Where k_i is the respiration rate at a soil depth z and re (m^{-1}) is a coefficient representing the impact of external factors, such

274 as oxygen availability that decreases with depth. k_0 is the respiration rate of the surface soil layer for a certain SOC pool i.

275 The variable re is determined in such a way that the total soil respiration of a certain pool over the entire soil profile

276 without erosion is similar to the output of the full ORCHIDEE model. Detailed description of how this is done can be

277 found in the study of Naipal et al. (2018).

278

279 **2.7 C erosion on hillslopes**

280

281 In the model we assume that soil erosion takes place on hillslopes, and not in the floodplains due to the usually low

282 topographical slope of floodplains. The factor *(1-f)* determines the fraction of the eroded soil that is deposited in the

283 colluvial reservoirs (Fig 1). Soil erosion always removes a fraction of the SOC stock in the upper soil layer depending on

284 the erosion rate and bulk density of the soil. The next soil layer contains less C and therefore at the following time-step less

285 C will be eroded under the same erosion rate. To account for this effect, the SOC profile evolution is dynamically tracked

286 in the model and updated at a daily time step, conform with the method of Wang et al. (2015). First, a fraction of the C

287 from each soil pool in proportion to the erosion height is removed from the surface layer. Then, at the same erosion rate,

288 SOC from the subsoil layer becomes the surface layer, maintaining the soil layer thickness in the vertical discretization

289 scheme. Similarly, the SOC from the subsoil later also moves upward one layer. The change in C content due to erosion of

290 the PFT-specific pools for hillslopes can be represented by the following equations:

291

292 $$\frac{dSOC_{HSi}(z,t)}{dt} = k_E * SOC_{HSi}(z+1,t) - k_E * SOC_{HSi}(z,t)$$ (14)

293

294 Where $dSOC_{HSi}(z,t)$ is the change in hillslope SOC of a component pool i at a depth z and at time step t. The daily erosion

295 fraction k_E (dimensionless) is calculated as following:

296

297 $$k_E = \frac{f*\left(\frac{E}{365}\right)}{BD*dz}$$ (15)

298

299 Where, E is the erosion rate (t ha^2 year $^{-1}$), f is the floodplain deposition factor, BD is the average bulk density of the soil

300 profile (g cm^{-3}) and dz is the soil thickness (=0.1 m).

301

302 This part of the model has been already applied at the global scale as the C removal model presented by Naipal et al.

303 (2018) and is here extended with the deposition term detailed above.

304

305 **2.8 C deposition and transport in floodplains**

306

307 The SOC profile dynamics of floodplains are controlled by: (1) C input from the hillslopes, (2) C import by lateral

308 transport from the floodplain fractions of upstream neighboring grid cells, and (3) C export to the floodplain fractions of

309 downstream neighboring grid cells (Fig 1). First, the net eroded flux from the surface layer of the hillslope fraction of the

310 grid cell (k_E *SOC$_{HS}$ (0)) is incorporated in the surface layer of the floodplain. At the same deposition rate, the SOC of the

311 surface layer of the floodplain is incorporated in the subsoil layer. Similarly, a fraction of the SOC of the subsoil layer is

312 moved downward one layer. It should be noted that C selectivity is not taken into account here, meaning that the C pools

313 of the deposited material are the same as the eroded material from the topsoil of eroding areas. At the same time a fraction

314 of the C of the surface layer proportional to the sediment residence time (τ) is exported out of the catchment following the

315 sediment routing scheme. This process represents the river bank erosion and resulting POC export by rivers. It should be

316 noted that rivers and streams are not explicitly represented in the model. As we do not have information on the sub-grid

317 spatial distribution of land cover fractions we first sum the exported C flux over all PFTs before assigning the flux

318 proportionally to the land cover fractions of the receiving downstream-lying grid cells. The C that is imported from the

319 neighboring grid cells follows the same procedure as the deposition of eroded material. The change in C content due to

320 deposition and river export/import of the PFT-specific pools for floodplains can be represented by the following equations:

321

322 $$\frac{dSOC_{FLi}(z,t)}{dt} = \left(\left(k_D + k_{i_{out}}\right)*SOC_{FLi}(z-1,t)\right) + \left(\frac{1}{(\tau*365)}*SOC_{FLi}(z+1,t)\right) - \left(\left(k_D + \frac{1}{(\tau*365)} + k_{i_{out}}\right)*SOC_{FLi}(z,t)\right),$$

323 for z>0 (16)

324

325 $$\frac{dSOC_{FLi}(0,t)}{dt} = \sum_{n=1}^{n=9}\left(k_{i_{out}}(n)*SOC_{FLi}(0,t)(n)\right) + \left(k_E*SOC_{HS_i}(0,t)\right) + \left(\frac{1}{(\tau*365)}*SOC_{FLi}(1,t)\right) - \left(\left(k_D + \frac{1}{(\tau*365)} + \right.\right.$$

326 $$\left.\left. k_{i_{out}}\right)*SOC_{FLi}(0,t)\right), \text{ for z=0}$$ (17)

327

328 Where *n* is the neighboring grid cell that flows into the current grid cell, $dSOC_{FLi}(z,t)$ is the change in floodplain SOC of a

329 component pool *i* at a depth *z* and at time step *t,* and SOC_{HS} is the hillslope SOC stock. k_D is the deposition rate and equal

330 to:

331

332 $k_D = \frac{k_E * AREA_{HS}}{AREA_{FL}}$ (18)

333

334 Where $AREA_{HS}$ is the hillslope area and $AREA_{FL}$ is the floodplain area (m^2). $k_{i_{out}}$ is the import rate per C pool *i* from

335 neighboring grid cells (dimensionless) and can be calculated as:

336

337 $k_{i_{out}} = \frac{\sum_{n=1}^{n=9}(W * \frac{1}{T*365} * AREA_{FL})\,(n)}{AREA_{FL}}$ (19)

338

339 Where, *W* is the weight index of equation 7.

340

341 **2.9 The land use change bookkeeping model**

342

343 The land use change bookkeeping scheme includes the yearly changes in forest, grassland and cropland areas in each grid

344 cell as reconstructed by Peng et al. (2017) (Table 1). Peng et al. (2017) derived historical changes in PFT fractions based

345 on LUHv2 land use dataset (Hurtt et al., 2011), historical forest area data from Houghton, and present day forest area from

346 ESA CCI satellite land cover (European Space Agency, ESA, 2014). By using different transition rules and independent

347 forest data to constrain the changes in crop and urban PFTs he derived the most suitable historical PFT maps.

348

349 When land use change takes place, the litter and SOC pools of all shrinking PFTs are summed and allocated proportionally

350 to the expanding PFTs, maintaining the mass-balance. In this way the litter pools and SOC stocks get impacted by different

351 input and respiration rates for each soil layer. When forest is reduced, three wood products with decay rates of 1, 10 and

352 100 years are formed and harvested. The biomass pools of other shrinking land cover types are transformed to litter and

353 allocated to the expanding PFTs. For more details on the land use scheme see the study of Naipal et al. (2018).

354

355 **2.10 Study-Area**

356

357 The model is tested for the Rhine catchment (Fig 2), which has a total basin area of 185,000 km^2 covering five different

358 countries in Central Europe. Its large size is beneficial for the application of a coarse-resolution model such as CE-

359 DYNAM to study large-scale regional dynamics in the C cycle due to soil erosion. The Rhine catchment has a very

360 interesting topography, with steep slopes larger than 20% upstream in the Alps, and large, wide and flat floodplains at the

361 foot of the Alps, the upper Rhine and the lower Rhine. The floodplains store large amounts of sediment and C that

362 originally was eroded from the steep hillslopes upstream. This makes it possible to study the long-term effect of erosion on

363   hillslope and floodplain dynamics. Furthermore, the Rhine catchment has been experiencing different stages of land use
364   change over the Holocene, with land degradation dating back to more than 5500 years ago (Dotterweich, 2013). In contrast,
365   during the last two decades there has been a general afforestation and soil erosion has been decreasing. These land use
366   changes and changes in erosion make an interesting and important case to study the effect of anthropogenic activities on
367   the C cycle in Europe.

368

369   In addition, the Rhine catchment has been the focus of many erosion studies providing observations on erosion and
370   sediment dynamics that can be used for model validation (Asselman, 1999; Asselman et al., 2003; Erkens, 2009; Hoffmann
371   et al., 2007, 2008, 2013a, 2013b; Naipal et al., 2016). The global sediment budget model that forms the basis for the
372   sediment dynamics of CE-DYNAM has been validated and calibrated for the Rhine catchment with observations on
373   sediment storage from Hoffmann et al. (2013b) and derived scaling relationships between sediment storage and basin area
374   (Naipal et al., 2016). These scaling relationships are also applicable for SOC storage and basin area. He found that for
375   floodplains the sediment and C storage increase in a non-linear way with basin area, while hillslopes show linear increase.
376   We will use these relationships to validate the spatial variability in SOC storage of floodplains and hillslopes simulated by
377   CE-DYNAM. The scaling relationships have the form of a simple power law:

378

379    $$M = a * (\frac{A}{A_{ref}})^b \qquad\qquad\qquad (20)$$

380

381   Where M is the sediment storage or the SOC storage, a is the storage (Mt) related to an arbitrary chosen area A_{ref}, while b is
382   the scaling exponent.

383

384   **2.11 Input data and model simulations**
385   To create the C emulator that forms the underlying C cycle part of CE-DYNAM, we first ran the full ORCHIDEE model
386   for the period 1850-2005 at a coarse resolution of 2.5°degrees latitude and 3.75° degrees longitude, and output all C pools
387   and fluxes. The pools and fluxes were then archived together and used to derive the turnover rates to build the emulator.
388   The SOC scheme of the emulator that has been modified to account for soil erosion processes has been made to run at a
389   spatial resolution of 5arcmin, similar to the original global sediment budget model. Then, we performed three main
390   simulations with CE-DYNAM for the Rhine catchment. Simulation S0: The baseline simulation or no-erosion simulation,
391   where SOC dynamics are similar to the full ORCHIDEE model. Simulation S1: The erosion -only simulation, where the
392   hillslopes erode and all eroded C is respired to the atmosphere without reaching the colluvial and alluvial deposition sites.
393   Simulation S2: The simulation with full sediment dynamics where hillslopes and floodplains are connected and can bury or
394   loose C. We ran the emulator for 2000 years at a daily time step with the initial climate and land cover of the period 1850-
395   1860. Afterwards, we performed the transient simulations for the period 1851-2005 at a daily time step with changing
396   climate and land cover conditions. However, after 2000 years the model the passive SOC pool was still not in complete
397   equilibrium with a change between 0.8 and 1 g C m^{-2} year^{-1}. Therefore, we subtracted the additional increase in SOC stocks
398   resulting from the disequilibrium state from the SOC stocks of the transient simulations before analyzing the transient
399   results.

400 Finally, to ensure a faster performance of CE-DYNAM we delineated the Rhine catchment in 7 large sub-basins based on
401 the flow direction and ran in parallel for each of the sub-basins at the daily timestep. After each year the sub-catchments
402 exchanged the C between each other.

403

404 **3 Results**

405

406 **3.1 Model validation**

407

408 We performed a detailed model validation of the sediment and the C part of the model based on the following steps: (1)
409 Validation of soil erosion rates using high-resolution model estimates and observations from other studies, (2) validation of
410 C erosion rates using high-resolution estimates for Europe from the study of Lugato et al. (2018), (3) validation of the
411 spatial variability of sediment storage, (4) validation of SOC stocks using data from a global soil database and a European
412 land use survey.

413

414 For the validation of gross soil erosion rates we used the high-resolution model estimates from the study of Panagos et al.
415 (2015), who applied the RUSLE2015 model at a 100 m resolution at European scale for the year 2010. The RUSLE2015 is
416 derived from the original RUSLE model with some modifications to the model parameters, especially the L, C and P
417 factors. We also used independent high-resolution erosion estimates from the study of Cerdan et al. (2010), which were
418 based on an extensive database of measured erosion rates under natural rainfall in Europe.

419

420 We show that the quantile distribution of our gross soil erosion rates fall in between the estimates of these two studies (Fig
421 3A&B). It should be noticed that our study and the study of Cerdan et al. (2010) simulated potential soil erosion rates, not
422 accounting for erosion control practices that are captured by the P-factor. We also compared the quantile distribution of our
423 net soil erosion rates from hillslopes with those of the study of Lugato et al. (2018), and show that they are similar (Fig
424 3C). Lugato et al. (2018) extended the RUSLE2015 model with a hillslope sediment deposition and transport scheme based
425 on the sediment delivery ratio concept.

426

427 For the comparison of the spatial variability of gross soil erosion rates we used the relationship of erosion to the
428 topographical slope and rainfall erosivity. These two parameters are argued to explain about 70% of the total potential soil
429 erosion rates at regional scales (Doetterl et al., 2012). We show that in our study and the study of Lugato et al. (2018)
430 erosion rates increase with increasing slope and erosivity, and that erosion can be high for very steep slopes with a low
431 erosivity (Fig 4). However, the difference between small and large erosion rates in our study is high, indicating an
432 underestimation of local variability in erosivity and slope. Overall, our results show that our coarse-resolution erosion
433 model is capable of producing reliable estimates of potential soil erosion rates and their spatial variability for the Rhine
434 catchment.

435

For the validation of gross C erosion rates, we used the results from Lugato et al. (2018), where they coupled the RUSLE2015 erosion model to the Century bio-geochemistry model. They provided an enhanced and a reduced erosion-induced C sink uncertainty scenario, based on different assumptions for C burial and C mineralization during transport. We find that the quantile distribution of our simulated erosion and deposition rates is close to that of Lugato et al. (2018) (Fig 5A-D). We also find that the relation between soil erosion and C erosion rates of our study is similar to the relation of Lugato et al. (2018) and falls within the uncertainty range (Fig 6). The coarse resolution of our model may explain the decreased variability between the estimates.

For the validation of SOC stocks we used the Global Dataset for Earth System Modeling (GSDE) (Shangguan et al., 2014) available at a spatial resolution of 1km and the Land Use/Land Cover Area Frame Survey (LUCAS) (Palmieri et al., 2011). The LUCAS topsoil SOC stocks, available at a high spatial resolution of 500 m, were calculated using the LUCAS SOC content for Europe (de Brogniez et al., 2015) and soil bulk density derived from soil texture datasets (Ballabio et al., 2016). We find that the simulated top 20 cm SOC stocks per land cover type generally fall within the quantile range of the LUCAS SOC stocks (Fig 7). We also find that the simulation with erosion does not substantially change this result but leads to slightly lower SOC stocks due to the impact of erosion and POC export out of the catchment. Furthermore, we find that in both the erosion and no-erosion simulation the SOC stocks for grassland are higher than for forest. This is also observed in the study of Wiesmeier et al. (2012) in South-Germany where they found considerable higher SOC stocks for grassland with a median of 11.8 kg C m^{-2} compared to forest based on the analysis of 1460 soil profiles.

To validate the spatial variability of SOC stocks we delineated 13 sub-basins in the non-Alpine region. We found a realistic spatial variability in topsoil SOC stocks after comparing our simulated SOC stocks from the erosion simulation with the SOC stocks of GSDE and LUCAS at sub-basin level (Table 2).

For the validation of sediment storage in hillslopes and on floodplains we used the same approach as in Naipal et al. (2016), where we based our validation on measured Holocene SOC deposits from the study of Hoffmann et al. (2013). Hoffmann et al. (2013) did an inventory of 41 hillslope and 36 floodplain sediment and SOC deposits related to soil erosion over the last 7500 years. They found that the sediment and SOC deposits were related to the basin size according to certain scaling functions, where floodplain deposits increased in a non-linear way with basin size while the hillslope deposits showed a linear increase with basin size. We selected the grid cells that contained the points of observation of the study of Hoffmann et al. (2013) and found a significantly larger exponent of the scaling relationship between floodplain SOC storage and basin area compared to hillslope SOC storage, which corresponds to the findings of Hoffmann et al. (2013). However, this is not the case when deriving the scaling relationships at sub-basins level (Table 3).

3.2 Model application

We find an average annual soil erosion rate of 4.66 t ha^{-1} year^{-1} over the period 1850-2005, which is 1.7 times larger than the average erosion rate simulated for the last millennium (Naipal et al., 2016) and 3.8 times larger than the average

473 erosion rate of the Holocene (Hoffmann et al., 2013). This soil erosion flux mobilized around 159 Tg of C over the period

474 1850-2005, of which 37% is deposited in colluvial reservoirs, 63% is deposited in alluvial reservoirs and 0.2% is exported

475 out of the catchment.

476

477 Over the period 1850-2005 there is a general afforestation in the Rhine catchment that started around 1920 AD (Fig 8B).

478 This afforestation takes place in the non-Alpine part of the Rhine and leads to a long-term decreasing trend in gross soil

479 and SOC erosion rates on hillslopes in the non-Alpine region (Fig 8D). In the Alpine part of the Rhine there was a

480 conversion of cropland and forest to grassland. Cropland decreases by 75% over the period 1920 and 1960, while forest

481 decreases by 16% over the period 1910-1950. The conversion of forest to grassland has a stronger impact on the soil

482 erosion rates than the conversion of cropland to forest, resulting in an increase of soil erosion rates over the period 1910-

483 1950 (Fig 8C). This increase is amplified by increased yearly precipitation in this region. Because the soil erosion rates in

484 the Alps are generally much larger than the soil erosion rates in the non-Alpine region due to the steep landscape, the

485 Alpine region dominates the trend in gross soil erosion and C erosion of the entire in the period 1910-1950 (Fig 8C). As a

486 result, the summed gross soil and C erosion rates over the whole Rhine catchment do not show a specific trend (Fig 8C).

487 The temporal variability in the soil and C erosion rates is a result of changes in precipitation (Fig 8A), however, land use

488 change dominates the overall long-term trend. Although precipitation is temporarily very variable, spatially it does not vary

489 significantly over the Rhine.

490

491 Furthermore, we find that the temporal variability in C erosion rates follow the soil erosion rates closely, indicating that

492 soil erosion dominates the variations in C erosion over this time-period, while increased SOC stocks due to CO_2

493 fertilization and afforestation play a secondary role as a slowly, varying trend.

494

495 We find that the cumulative C erosion removal flux of 159 Tg leads to a cumulative net C sink of 90 Tg C for the whole

496 Rhine region (Fig 8E). This is about 1% of the cumulative NPP and about one fourth of the cumulative land C sink of the

497 Rhine without erosion. For the non-Alpine part of the Rhine, erosion leads to a net C sink of 55 Tg C, which equals to one

498 fifth of the total land C sink without erosion. It should be noted that these are potential fluxes, assuming that the

499 photosynthetic replacement of C is not affected by the degradation of soil due to the removal of nutrients, declining water-

500 holding capacity and other negative changes to the soil structure and texture (processes not covered by our model). The

501 breaking point in the graphs of figure 8E and F around 1910AD is a result of the climate data used as input.

502

503 To better understand the erosion-induced net C flux (Fig 8E, F), we analyzed the erosion-induced C exchange with the

504 atmosphere by creating C budgets for the entire Rhine catchment for the period 1850-1860 and for the period 1950-2005

505 (Fig 9A&B). These C budgets also shed light on changes in the linkage between lateral and vertical C fluxes over time. As

506 we do not explicitly track the movement of eroded C through all reservoirs (for example between eroding hillslopes and

507 colluvial reservoirs), we make use of the changes in SOC stocks and NEP of the three main simulations (S0, S1, S2) to

508 derive the erosion-induced vertical C fluxes.

509

510   By subtracting the Net Ecosystem Productivity of hillslopes (NEP_{HS}), which is the difference between NPP and

511   heterotrophic respiration, of the no-erosion simulation (S0) from the erosion-only simulation (S1), we derive the additional

512   photosynthetic replacement of SOC on eroding sites (eq 21):

514    $$E_{rep} = NEP_{HS}(S1) - NEP_{HS}(S0) \qquad (21)$$

516   Where, E_{rep} is the potential dynamic Photosynthetic replacement of C on eroding sites (assuming no feedback of erosion on

517   NPP). Part of the eroded C that is transported to and deposited in colluvial reservoirs can be respired or buried (Eq. 22).

518   The difference between NEP of simulation S2 and S1 is the NEP caused by the deposition of eroded C in colluvial areas

519   and equal to the difference between the burial and respiration of C in colluvial sites. As we do not explicitly track the

520   respiration of deposited material in the model, we can only derive the net respiration or net burial of the colluvial deposits

521   (Rc_{net}) with the following equation:

523    $$Rc_{net} = NEP_{HS}(S2) - NEP_{HS}(S1) \qquad (22)$$

525   The same concept can be applied for the net respiration of floodplains:

527    $$Ra_{net} = NEP_{FL}(S2) - NEP_{FL}(S0) \qquad (23)$$

529   Where, NEP_{FL} is the floodplain Net Ecosystem Productivity, and Ra_{net} is the net respiration or net burial of alluvial

530   deposits. Positive values for Ra_{net} or Rc_{net} indicate a net burial (respiration S2 < respiration S0/S1) of the deposited

531   material. We find that dynamic replacement of C on eroding sites increased by 39% at the end of the period despite

532   decreasing soil erosion rates (Fig 9A&B). This increase in the photosynthetic replacement of C is due to the globally

533   increasing CO_2 concentrations known as the CO2 fertilization effect, amplified by the afforestation trend in the Rhine over

534   this period. Without this fertilization effect, soil erosion and deposition would be likely a weaker C sink or even a C source

535   over the period 1850-2005. Furthermore, we find that the yearly average gross C erosion flux from eroding sites decreased

536   slightly by 2%, while the yearly deposition fluxes in colluvial and alluvial sites decreased by 3.5 % and 0.6%, respectively.

537   The decrease in the deposition flux to floodplains is compensated by better sediment connectivity between hillslopes and

538   floodplains due to afforestation. Forests have less man-made structures that can prevent the erosion fluxes from reaching

539   the floodplains, which is represented by a higher floodplain deposition 'f' factor in the model.

541   We also find that colluvial reservoirs show a net respiration flux throughout the time period (Fig 9A&B). This is consistent

542   with previous studies who found that colluvial sites can be areas of increased CO_2 emissions (Billings et al., 2019; Van

543   Oost et al., 2012). However, the difference between the start and end of the transient period is triggered by the net

544   respiration/burial flux of deposited C in floodplains. While at the start of the period, deposition in alluvial reservoirs leads

545   to a substantial net burial flux (~0.8 times the floodplain deposition), at the end of the period respiration of deposited SOC

546   in floodplains is larger than this burial flux (Fig 9B). This is a result of an increased respiration of deposited material over

547 the entire catchment, most likely due to increasing temperatures over 1850-2005. The constant removal of C-rich topsoil

548 and its deposition in alluvial and colluvial reservoirs makes the deposited sediments generally richer in C than soils on

549 erosion-neutral sites, providing more substrate for respiration. The largest increase in total respiration of alluvial and

550 colluvial deposits takes place in the Alps due to the initial increase in erosion rates resulting in large deposits of C.

551

552 We also observe declining erosion rates over the non-Alpine region leading to decreasing or less strong increasing dynamic

553 replacement of C. Both processes, the decrease in burial dynamic C replacement, contribute to a reduced increase in the

554 erosion-induced net C sink over time (Fig 8E, F).

555

556 4 Discussion

557

558 4.1 Initial conditions and past global changes

559

560 Initial climate and land cover/use conditions needed to perform the equilibrium simulation together with the length of the

561 transient period are essential parameters that determine the resulting spatial distribution of soil and C. Landscapes are in a

562 constant transient state due to global changes, such as climate change, land use change, accelerated soil erosion. However,

563 we assumed an equilibrium state so that we can quantify the changes during the transient period. The more one goes back

564 in time to select the initial conditions and the longer the transient period that covers the essential historical environmental

565 changes, the more accurate are the present-day distribution of SOC stocks, sediment storages, and related fluxes. This is

566 especially true when analyzing the redistribution of soil and C as a result of erosion, deposition and transport, as these soil

567 processes can be very slow. For example, the study of Naipal et al. (2016) shows that by simulating the soil erosion

568 processes for the last millennium a spatial distribution of sediment storages that is similar to observations can be found. In

569 this study we modeled steady state initial conditions of the period 1850-1860 due to constrains in data availability on

570 precipitation and temperature, and because the aim of this study is to present the potential and limitations of CE-DYNAM

571 rather than provide precise values for soil and C stocks and fluxes. By focusing only on the period 1850-2005 we miss the

572 effects of significant land use changes in the past that coincided with times of strong precipitation such as in the 14th and

573 18th century. These major anthropogenic changes in the last Holocene substantially affected the present-day spatial

574 distribution and size of SOC stocks. As a result, we find that floodplains store less SOC than hillslopes at the end of the

575 transient period (Fig 10A), which is different from the findings of Hoffmann et al. (2013) and what can be derived from

576 global soil databases. Hoffmann et al. (2013) showed that the large amount of C stored in the deeper layers of the

577 floodplains can be several thousands of years old. In addition, the high C stocks in floodplains also result from higher local

578 plant productivity due to favorable soil nutrient and hydrological conditions. In our study we do not capture this effect and

579 we do not look at a timescale long enough to capture this distinction between SOC storage in floodplains and in hillslopes.

580 However, we did not find that the vertical distribution of C in floodplain sediment is more homogenous or shows a less

581 strong decrease in C with depth (Fig 10B). This is in line with the findings of previous studies (Hoffmann et al., 2013;

582 Billings et al., 2019).

583

4.2 Model limitations

Although CE-DYNAM explicitly account for hillslope and floodplains re-deposition, it neglects important processes affecting the C dynamics in floodplains. The model does not account for a slower respiration rate due to low-oxygen conditions, physical and chemical stabilization (Berhe et al., 2008; Martínez-mena et al., 2019) or a higher NPP for nutrient-rich floodplains (Van Oost et al., 2012; Hoffmann et al., 2013). The oxidation and preservation of C in deposition environments, especially in alluvial reservoirs remain highly uncertain (Billings et al., 2019). Furthermore, the model does not take into account the selectivity of erosion, often expressed as the enrichment ratio, where the C content of eroding soil can be higher than that of the original soil. The enrichment ratio can be very variable across landscapes, while the importance of erosion selectivity for C is still under debate (Nadeu et al., 2015; Wang et al., 2010).

CE-DYNAM does not account for different ratios between the SOC pools (active, slow, passive) with depth due to the limitation in information to constrain these fractions for floodplains and hillslopes. However, this can be potentially important for respiration of C in depositional sites and during transport. Studies show that the labile C is decomposed first during sediment transport and directly after deposition, leaving behind the more recalcitrant C in deposition sites (Berhe et al., 2007; Billings et al., 2019). Due to the simplistic nature of our coarse-resolution model and the lack of data on oxidation of eroded C during transport we did not include C respiration during transport in the model. We also do not take into account the transformation of POC to DOC and their fate in rivers and streams. The model also lacks dams in and fixed river banks of the Rhine river. In this way, CE-DYNAM provides only a potential state of soil and SOC redistribution as would be under more natural conditions. Furthermore, there is no feedback between soil erosion and plant productivity in the model. To account for such process soil erosion processes would need to be explicitly included in a land surface model such as ORCHIDEE. The lack of this feedback results in an unlimited dynamic replacement of C on eroding sites.

5 Conclusions

We presented a novel spatially-explicit and process-based C erosion dynamics model, CE-DYNAM, which simulates the redistribution of soil and C over land as a result of water erosion and calculates the role of this redistribution for C budgets at catchment scale. We demonstrate that CE-DYNAM captures the spatial variability in soil erosion, carbon erosion and SOC stocks of the Rhine catchment when compared to high-resolution estimates and observations. We also show that the quantile ranges of erosion and deposition rates and C stocks fall within the uncertainty ranges of previous estimates at basin or sub-basin level. Furthermore, we demonstrate the model ability to disentangle vertical C fluxes resulting from the redistribution of C over land and develop C budgets that can shed light on the role of erosion in the C cycle. The simple structure of CE-DYNAM and the relative low amount of parameters makes it possible to run several simulations to investigate the role of individual processes on the C cycle such as removal by erosion only, or the role of deposition and transport. Its compatibility with land surface models makes it possible to investigate the long-term and large-scale effect of erosion processes under various global changes such as increasing atmospheric CO_2 concentrations, changes to precipitation and temperature, and land use change.

The application of CE-DYNAM for the Rhine catchment for the period 1850-2005 AD reveals three key findings:

- Soil erosion leads to a cumulative net C sink of 90 Tg by the end of the period, which is equal to one fourth of the cumulative land C sink of the Rhine without erosion. This C sink is a result of an increasing dynamic replacement of C on eroding sites due to the CO_2 fertilization effect, despite decreasing soil and C erosion rates over the largest part of the catchment. We conclude that it is important to take global changes such as climate change into account to better quantify the net effect of erosion on the C cycle.

- The erosion-induced C sink decreases over time due to decreasing erosion rates and increasing respiration of deposited C in alluvial and colluvial reservoirs. In contrast to colluvial reservoirs, alluvial reservoirs experience a net C burial. However, this net C burial can become net C respiration due to changes in the climate such as global warming. We conclude that burial of eroded C in floodplains plays an essential role in the strength of the erosion-induced C sink.

- Initial climate and land cover conditions and the transient period over which erosion under global changes takes place are essential for the determination if soil erosion is a net C sink or source and to what extent.

Altogether, these results indicate that despite model uncertainties related to the relative coarse spatial resolution, missing or simplified processes, CE-DYNAM represents an important step forwards into integrating soil erosion processes and sediment dynamics in Earth system models.

Code and data availability

The source code of CE-DYNAM is included as a supplement to this paper. Model data can be accessed from the Zenodo repository under the doi:10.5281/zenodo.2642452 (not published yet). For the other data sets that are listed in Table 1, it is encouraged to contact the first authors of the original references.

Author contributions

VN built and implemented the mode. YW provided the basic structure for the model. All authors contributed in the interpretation of the results and wrote the paper.

Competing interests

The authors declare that they have no conflict of interest.

Acknowledgements

657   Funding was provided by the Laboratory for Sciences of Climate and Environment (LSCE), CEA, CNRS, and UVSQ.
658   Victoria Naipal, Ronny Lauerwald and Philippe Ciais acknowledges support from the VERIFY project that received
659   funding from the European Union's Horizon 2020 research and innovation program under grant agreement No 776810.
660   Bertrand Guenet acknowledges support from the project ERANETMED2-72-209 ASSESS. We also thank Dr. S. Peng for
661   sharing the PFT maps.

662

663   **References**

664

665   Asselman, N. E. M.: Suspended sediment dynamics in a large drainage basin : the River Rhine , 1450(November 1998),
666   1437–1450, https://doi.org/10.1002/(SICI)1099-1085(199907)13:10<1437::AID-HYP821>3.0.CO;2-J ,1999.

667

668   Asselman, N. E. M., Middelkoop, H. and van Dijk, P. M.: The impact of changes in climate and land use on soil erosion,
669   transport and deposition of suspended sediment in the River Rhine, Hydrol. Process., 17(16), 3225–3244,
670   doi:10.1002/hyp.1384, 2003.

671

672   Ballabio, C., Panagos, P. and Monatanarella, L.: Geoderma Mapping topsoil physical properties at European scale using
673   the LUCAS database, Geoderma, 261, 110–123, doi:10.1016/j.geoderma.2015.07.006, 2016.

674

675   Berhe, A. A., Harte, J., Harden, J. W. and Torn, M. S.: The Significance of the Erosion-induced Terrestrial Carbon Sink,
676   Bioscience, 57(4), 337, doi:10.1641/B570408, 2007.

677

678   Berhe, A. A., Harden, J. W., Torn, M. S. and Harte, J.: Linking soil organic matter dynamics and erosion-induced
679   terrestrial carbon sequestration at different landform positions, J. Geophys. Res. Biogeosciences, 113(4), 1–12,
680   doi:10.1029/2008JG000751, 2008.

681

682   Billings, S. A., Richter, D. D. B., Ziegler, S. E., Prestegaard, K. and Wade, A. M.: Distinct Contributions of Eroding and
683   Depositional Profiles to Land-Atmosphere CO_2 Exchange in Two Contrasting Forests, 7(March),
684   doi:10.3389/feart.2019.00036, 2019.

685

686   de Brogniez, D., Ballabio, C., Stevens, A., Jones, R. J. A., Montanarella, L. and Van Wesemael, B.: A map of the topsoil
687   organic carbon content of Europe generated by a generalized additive model, Eur. J. Soil Sci., 66(January), 121–134,
688   doi:10.1111/ejss.12193, 2015.

689

690   Cerdan, O., Govers, G., Le Bissonnais, Y., Van Oost, K., Poesen, J., Saby, N., Gobin, a., Vacca, a., Quinton, J.,
691   Auerswald, K., Klik, a., Kwaad, F. J. P. M., Raclot, D., Ionita, I., Rejman, J., Rousseva, S., Muxart, T., Roxo, M. J. and
692   Dostal, T.: Rates and spatial variations of soil erosion in Europe: A study based on erosion plot data, Geomorphology,
693   122(1–2), 167–177, doi:10.1016/j.geomorph.2010.06.011, 2010.

694

695 Ciais, P., Sabine, C., Bala, G., Bopp, L., Brovkin, V., Canadell, J., Chhabra, A., DeFries, R., Galloway, J., Heimann, M.,
696 Jones, C., Quéré, C. Le, Myneni, R. B., Piao, S. and Thornton, P.: Carbon and Other Biogeochemical Cycles, in Climate
697 Change 2013: The physical science basis. Contribution of working group I to the fifth assessment report of the
698 intergovernmental panel on climate change [Stocker, T.F., D. Qin, G.-K. Plattner, M. Tignor, S.K. Allen, J. Boschung, A.
699 Nauels, Y. Xia, pp. 465–570, Cambridge University Press, Cambridge, United Kingdom and New York, NY., 2013.
700

701 Doetterl, S., Van Oost, K. and Six, J.: Towards constraining the magnitude of global agricultural sediment and soil organic
702 carbon fluxes, Earth Surf. Process. Landforms, doi:10.1002/esp.3198, 2012.
703

704 Dotterweich, M.: Geomorphology The history of human-induced soil erosion : Geomorphic legacies , early descriptions
705 and research , and the development of soil conservation — A global synopsis, Geomorphology, 201(November), 1–34,
706 doi:10.1016/j.geomorph.2013.07.021, 2013.
707

708 Erkens, G.: Sediment dynamics in the Rhine catchment, Utrecht University, Faculty of Geosciences, Utrecht., 2009.
709

710 Frieler, K., Lange, S., Piontek, F., Reyer, C. P. O., Schewe, J., Warszawski, L., Zhao, F., Chini, L., Denvil, S., Emanuel,
711 K., Geiger, T., Halladay, K., Hurtt, G., Mengel, M., Murakami, D., Ostberg, S., Popp, A. and Riva, R.: Assessing the
712 impacts of 1 . 5 ◦ C global warming – simulation protocol of the Inter-Sectoral Impact Model Intercomparison Project (
713 ISIMIP2b), Geosci. Model Dev., 10, 4321–4345, 2017.
714

715 Hay R.K.M.: Harvest index: a review of its use in plant breeding and crop physiology, Ann. appl. Biol., 126, 197–216,
716 1995.
717

718 Hoffmann, T., Erkens, G., Cohen, K. M., Houben, P., Seidel, J. and Dikau, R.: Holocene floodplain sediment storage and
719 hillslope erosion within the Rhine catchment, The Holocene, 17(1), 105–118, doi:10.1177/0959683607073287, 2007.
720

721 Hoffmann, T., Lang, a and Dikau, R.: Holocene river activity: analysing 14C-dated fluvial and colluvial sediments from
722 Germany, Quat. Sci. Rev., 27(21–22), 2031–2040, doi:10.1016/j.quascirev.2008.06.014, 2008.
723

724 Hoffmann, T., Schlummer, M., Notebaert, B., Verstraeten, G. and Korup, O.: Carbon burial in soil sediments from
725 Holocene agricultural erosion, Central Europe, Global Biogeochem. Cycles, 27(3), 828–835, doi:10.1002/gbc.20071,
726 2013a.
727

728 Hoffmann, T., Mudd, S. M., van Oost, K., Verstraeten, G., Erkens, G., Lang, a., Middelkoop, H., Boyle, J., Kaplan, J. O.,
729 Willenbring, J. and Aalto, R.: Short Communication: Humans and the missing C-sink: erosion and burial of soil carbon
730 through time, Earth Surf. Dyn., 1(1), 45–52, doi:10.5194/esurf-1-45-2013, 2013b.

731

732 Hurtt, G. C., Chini, L. P., Frolking, S., Betts, R. A., Feddema, J. and Fischer, G.: Harmonization of land-use scenarios for
733 the period 1500 – 2100 : 600 years of global gridded annual land-use transitions , wood harvest , and resulting secondary
734 lands, Clim. Chang., 109, 117–161, doi:10.1007/s10584-011-0153-2, 2011.

735

736 Krinner, G., Viovy, N., de Noblet-Ducoudré, N., Ogée, J., Polcher, J., Friedlingstein, P., Ciais, P., Sitch, S. and Prentice, I.
737 C.: A dynamic global vegetation model for studies of the coupled atmosphere-biosphere system, Global Biogeochem.
738 Cycles, 19(1), 1–33, doi:10.1029/2003GB002199, 2005.

739

740 Lal, R.: Soil erosion and the global carbon budget., Environ. Int., 29(4), 437–50, doi:10.1016/S0160-4120(02)00192-7,
741 2003.

742

743 Lehner, B. and Grill, G.: Global river hydrography and network routing : baseline data and new approaches to study the
744 world ' s large river systems, Hydrol. Process., 2186(April), 2171–2186, doi:10.1002/hyp.9740, 2013.

745

746 Ludwig, W. and Probst, J.-L.: River Sediment Discharge to the Oceans: Present-Day Controls and Global Budgets, Am. J.
747 Sci., 298(April), 265–295, 1998.

748

749 Lugato, E., Smith, P., Borrelli, P., Panagos, P., Ballabio, C., Orgiazzi, A., Fernandez-ugalde, O., Montanarella, L. and
750 Jones, A.: Soil erosion is unlikely to drive a future carbon sink in Europe, Sci. Adv., 4(November), eaau3523, 2018.

751

752 Martínez-mena, M., Almagro, M., García-franco, N., Vente, J. De and García, E.: Fluvial sedimentary deposits as carbon
753 sinks : organic carbon pools and stabilization mechanisms across a Mediterranean catchment, 1035–1051, 2019.

754

755 Mayorga, E., Seitzinger, S. P., Harrison, J. a., Dumont, E., Beusen, A. H. W., Bouwman, a. F., Fekete, B. M., Kroeze, C.
756 and Van Drecht, G.: Global Nutrient Export from WaterSheds 2 (NEWS 2): Model development and implementation,
757 Environ. Model. Softw., 25(7), 837–853, doi:10.1016/j.envsoft.2010.01.007, 2010.

758

759 Nadeu, E., Gobin, A., Fiener, P., van Wesemael, B. and van Oost, K.: Modelling the impact of agricultural management on
760 soil carbon stocks at the regional scale: the role of lateral fluxes., Glob. Chang. Biol., 21(8), 3181–92,
761 doi:10.1111/gcb.12889, 2015.

762

763 Naipal, V., Reick, C., Pongratz, J. and Van Oost, K.: Improving the global applicability of the RUSLE model - Adjustment
764 of the topographical and rainfall erosivity factors, Geosci. Model Dev., 8(9), doi:10.5194/gmd-8-2893-2015, 2015.

765

766 Naipal, V., Reick, C., Van Oost, K., Hoffmann, T. and Pongratz, J.: Modeling long-term, large-scale sediment storage
767 using a simple sediment budget approach, Earth Surf. Dyn., 4, 407–423, doi:10.5194/esurf-4-407-2016, 2016.

768

769   Naipal, V., Ciais, P., Wang, Y., Lauerwald, R., Guenet, B. and Oost, K. Van: Global soil organic carbon removal by water
770   erosion under climate change and land use change during AD 1850 – 2005, Biogeosciences, 15(July), 4459–4480,
771   doi:https://doi.org/10.5194/bg-15-4459-2018, 2018.

772

773   Van Oost, K., Quine, T. a, Govers, G., De Gryze, S., Six, J., Harden, J. W., Ritchie, J. C., McCarty, G. W., Heckrath, G.,
774   Kosmas, C., Giraldez, J. V, da Silva, J. R. M. and Merckx, R.: The impact of agricultural soil erosion on the global carbon
775   cycle., Science, 318(5850), 626–9, doi:10.1126/science.1145724, 2007.

776

777   Van Oost, K., Verstraeten, G., Doetterl, S., Notebaert, B., Wiaux, F. and Broothaerts, N.: Legacy of human-induced C
778   erosion and burial on soil – atmosphere C exchange, PNAS, 109(47), 19492–19497, doi:10.1073/pnas.1211162109/-
779   /DCSupplemental.www.pnas.org/cgi/doi/10.1073/pnas.1211162109, 2012.

780

781   Palmieri, A., Martino, L., Dominici, P. and Kasanko, M.: Land Cover and Land Use Diversity Indicatorsin LUCAS 2009
782   data., 2011.

783

784   Panagos, P., Borrelli, P., Poesen, J., Ballabio, C., Lugato, E., Meusburger, K., Montanarella, L. and Alewell, C.:
785   Environmental Science & Policy The new assessment of soil loss by water erosion in Europe, Environ. Sci. Policy, 54,
786   438–447, doi:10.1016/j.envsci.2015.08.012, 2015.

787

788   Panagos, P., Borrelli, P., Meusburger, K., Yu, B., Klik, A., Lim, K. J., Yang, J. E., Ni, J., Miao, C., Chattopadhyay, N.,
789   Sadeghi, S. H., Hazbavi, Z., Zabihi, M., Larionov, G. A., Krasnov, S. F., Gorobets, A. V., Levi, Y., Erpul, G., Birkel, C.,
790   Hoyos, N., Naipal, V., Oliveira, P. T. S., Bonilla, C. A., Meddi, M., Nel, W., Al Dashti, H., Boni, M., Diodato, N., Van
791   Oost, K., Nearing, M. and Ballabio, C.: Global rainfall erosivity assessment based on high-temporal resolution rainfall
792   records, Sci. Rep., 7(1), doi:10.1038/s41598-017-04282-8, 2017.

793

794   Parton, W. J., Schimel, D. S., Cole, C. V. and Ojima, D. S.: Analysis of Factors Controlling Soil Organic Matter Levels in
795   Great Plains Grasslands1, Soil Sci. Soc. Am. J., 51(5), 1173, doi:10.2136/sssaj1987.03615995005100050015x, 1987.

796

797   Pelletier, J. D., Broxton, P. D., Hazenberg, P., Zeng, X., Troch, P. A., Niu, G. Y., Williams, Z., Brunke, M. A. and Gochis,
798   D.: A gridded global data set of soil, intact regolith, and sedimentary deposit thicknesses for regional and global land
799   surface modeling, J. Adv. Model. Earth Syst., doi:10.1002/2015MS000526, 2016.

800

801   Peng, S., Ciais, P., Maignan, F., Li, W., Chang, J., Wang, T. and Yue, C.: Sensitivity of land use change emission estimates
802   to historical land use and land cover mapping, Global Biogeochem. Cycles, 31(4), 626–643, doi:10.1002/2015GB005360,
803   2017.

804

805   Renard, K.G., Foster, G.R., Weesies, G.A., McCool, D.K., Yoder, D. C.: Predicting Soil Erosion by Water: A Guide to
806   Conservation Planning with the Revised Universal Soil Loss Equation (RUSLE), United States Department of Agriculture,
807   Washington, DC., 1997.

808

809   Schauberger, B., Ben-ari, T., Makowski, D., Kato, T., Kato, H. and Ciais, P.: Yield trends , variability and stagnation
810   analysis of major crops in France over more than a century, Sci. Rep., (November), 1–12, doi:10.1038/s41598-018-35351-
811   1, 2018.

812

813   Shangguan H.W., Dai Y., Duan Q., Liu B., Y. H.: A global soil data set for earth systemmodeling Wei, J. Adv. Model.
814   Earth Syst., 6, 249–263, 2014, doi:10.1002/2013MS000293.

815

816   Stallard, R. F.: Terrestrial sedimentation and the carbon cycle : Coupling weathering and erosion to carbon burial, Global
817   Biogeochem. Cycles, 12(2), 231–257, 1998.

818

819   Thonicke, K., Spessa, A., Prentice, I. C., Harrison, S. P. and Dong, L.: The influence of vegetation , fire spread and fire
820   behaviour on biomass burning and trace gas emissions : results from a process-based model, Biogeosciences, 7, 1991–
821   2011, doi:10.5194/bg-7-1991-2010, 2010.

822

823   Wang, Z., Govers, G., Steegen, A., Clymans, W., Putte, A. Van Den, Langhans, C., Merckx, R. and Oost, K. Van:
824   Geomorphology Catchment-scale carbon redistribution and delivery by water erosion in an intensively cultivated area,
825   Geomorphology, 124(1–2), 65–74, doi:10.1016/j.geomorph.2010.08.010, 2010.

826

827   Wang, Z., Doetterl, S., Vanclooster, M., van Wesemael, B. and Van Oost, K.: Constraining a coupled erosion and soil
828   organic carbon model using hillslope-scale patterns of carbon stocks and pool composition, J. Geophys. Res.
829   Biogeosciences, 120, 452–465, doi:10.1002/2014JG002768, 2015.

830

831   Wang, Z., Hoffmann, T., Six, J., Kaplan, J. O., Govers, G., Doetterl, S. and Van Oost, K.: Human-induced erosion has
832   offset one-third of carbon emissions from land cover change, Nat. Clim. Chang., 7(5), 345–349, doi:10.1038/nclimate3263,
833   2017.

834

835   Wiesmeier, M., Sporlein, P., Geuß, U. W. E., Hangen, E., Haug, S., Reischl, A., Schilling, B., Lutzow, M. V. O. N. and
836   Kogel-Knaber, I.: Soil organic carbon stocks in southeast Germany (Bavaria) as affected by land use , soil type and
837   sampling depth, Glob. Chang. Biol., (March), 1–13, doi:10.1111/j.1365-2486.2012.02699.x, 2012.

838

839

840

841

842 **Table 1:** Model input datasets

Dataset	Spatial resolution	Temporal resolution	Period	Source
Historical land cover and land use change	0.25 degrees	annual	1850-2005	Peng et al. (2017)
Climate data (precipitation & temperature) for ORCHIDEE	0.5 degrees	6 hourly	1900-2012	CRU-NCEP version 5.3.2; https://crudata.uea.ac.uk/ cru/data/ncep/; last access: 5 April 2019
precipitation for the Adj. RUSLE	0.5 degrees	monthly	1850-2005	ISIMIP2b (Frieler et al., 2017)
Soil	1 km	-	-	Global Soil Dataset for Earth System Modeling, GSDE (Shangguan H.W., Dai Y., Duan Q., Liu B., 2014)
Topography	30 arcseconds	-	-	GTOPO30; U.S. Geological Survey, EROS Data Center Distributed Active Archive Center 2004; https://www.ngdc.noaa.gov/mgg/topo/gltile s.html; last access: 5 April 2019
Flow accumulation	30 arcseconds	-	-	HydroSHEDS (Lehner et al., 2013); https://www.hydrosheds.org/; last access: 5 April 2019
Hillslopes/Floodplain area	5 arcminutes	-	-	Pelletier et al. (2016)
River network & stream length	30 arcseconds	-	-	Hydrosheds (Lehner et al., 2008)

843
844

845 **Table 2:** This table shows the results of the linear regression between the simulated total SOC stocks (Tg of C per year)
846 and those of the Global Soil dataset for Earth System Modeling (GSDE) and from the LUCAS database. The regression is
847 done after aggregating the data at sub-basin level for the 13 sub-basins that were delineated in the Rhine catchment.
848 RMSE is the root mean square error given in Tg of C per year, while the r-value is the spatial correlation coefficient.

Regression	r-value	p-value	RMSE
This study versus LUCAS	0.96	<0.01	28.69
This study versus GSDE	0.95	<0.01	29.32

849
850

851 **Table 3**: This table presents the scaling exponent (b) of equation 20 for floodplains and hillslopes. The scaling exponent
852 was derived for selected points in the Rhine catchment for which measurements on the SOC storage were taken by
853 Hoffmann et al. (2013), and at sub-basin level after the data on area and SOC stocks was aggregated for each of the 13 sub-
854 basins of the Rhine.

	Scaling exponent floodplains	Scaling exponent hillslopes
Hoffmann et al. (2013)	1.23±0.06	1.08±0.07

This study (selected points where measurements were taken)	1.14	0.83
This study (based on the 13 sub-basins)	1.06	1.00

855

856

857
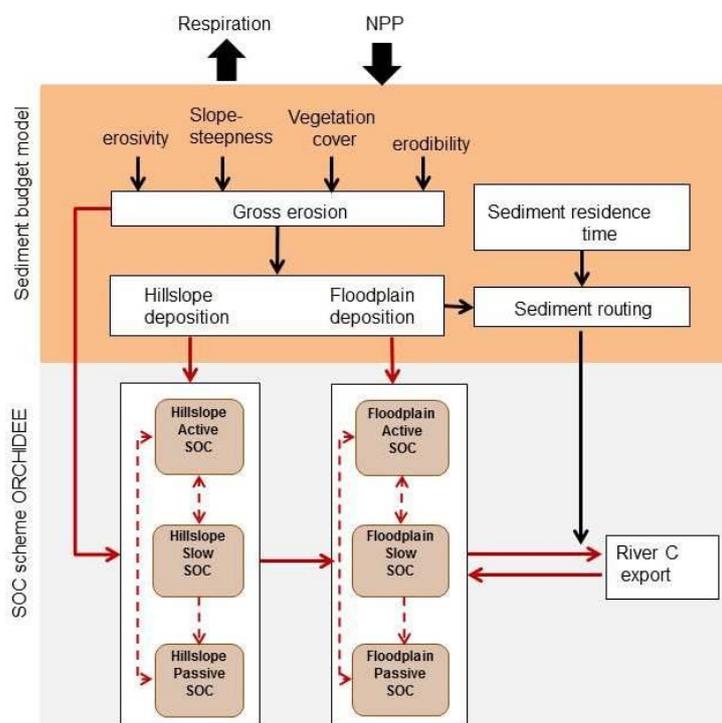
858 **Figure 1:** A conceptual diagram of CE-DYNAM. The red arrows represent the C fluxes between the C pools/reservoirs,

859 while the black arrows represent the link between the erosion processes (removal, deposition and transport).
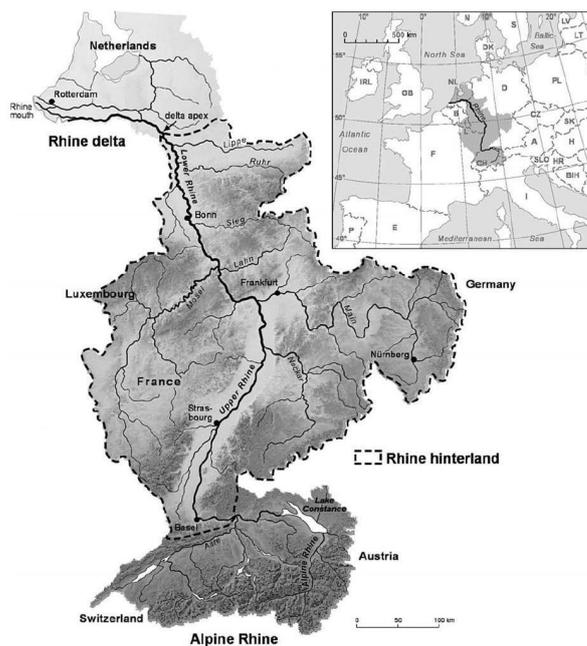
860
861   **Figure 2:** The Rhine catchment (Hoffmann et al., 2013)

862
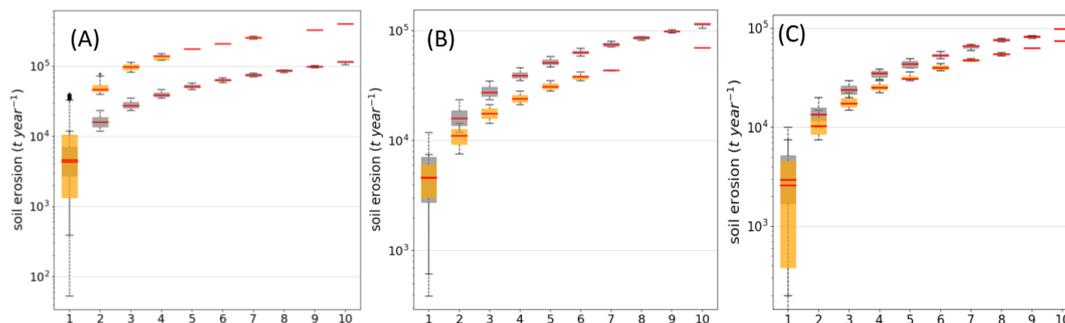
863

864   **Figure 3**: Quantile-whisker plot of simulated **gross** soil erosion rates (t/year) (grey whisker boxes), compared to (A) the
865   study of Cerdan et al. (2010) and (B) the study of Panagos et al. (2015) (orange whisker boxes). (C) Quantile-whisker plot
866   of simulated **net** soil erosion rates (t/year) (grey whisker boxes), compared to the study of Borrelli et al. (2018) (orange
867   whisker boxes). Medians are plotted as red horizontal lines.
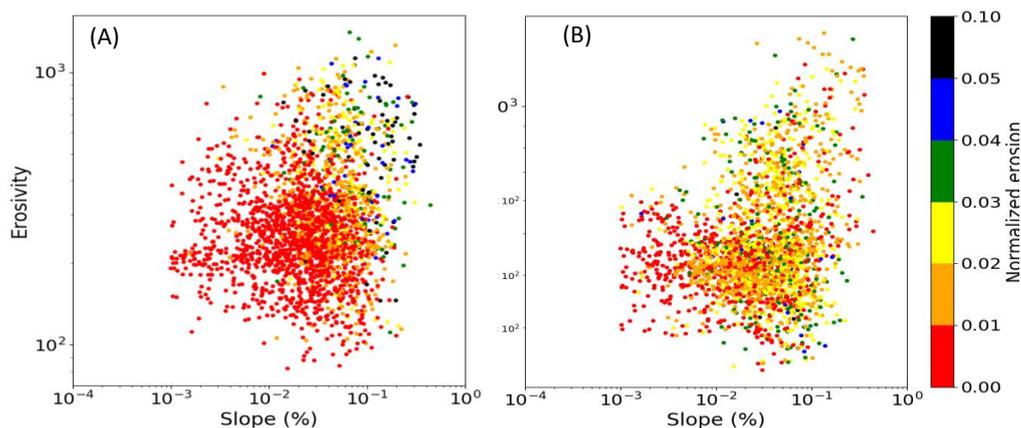
868

869 **Figure 4**: Normalized gross soil erosion as a function of the topographical slope (%) and rainfall erosivity for (A) this
870 study and (B) RUSLE2015
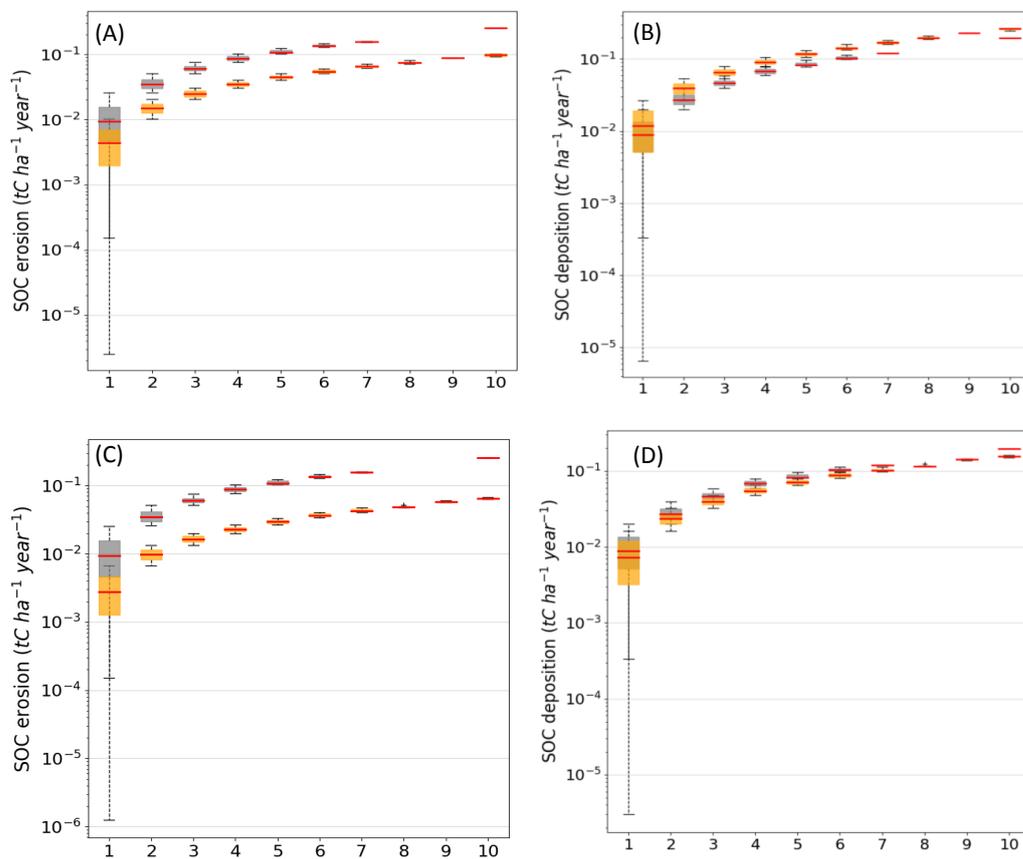
871

872

873 **Figure 5**: (A) Hillslope C erosion rates and, (B) C deposition rates, compared to the enhanced erosion scenario from
874 Lugato et al. (2018). (C) Hillslope C erosion rates and, (D) C deposition rates, compared to the reduced erosion scenario
875 from Lugato et al. (2018).
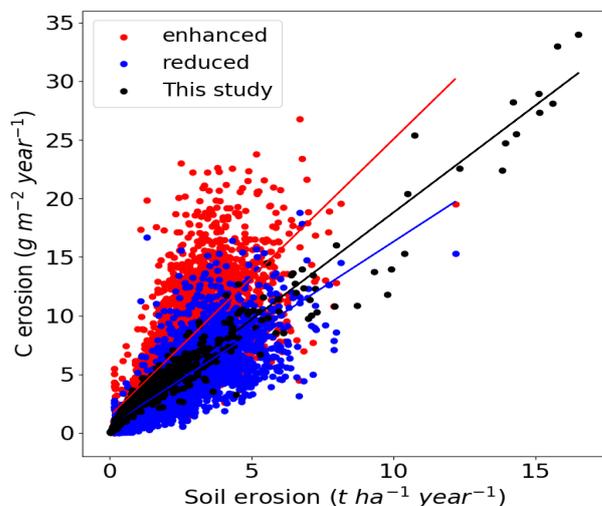
876

877 **Figure 6**: The relationship between soil erosion and C erosion of simulation S2 (black points) in comparison to the erosion
878 scenarios from the study of Lugato et al. (2018) with enhanced (red points) and reduced erosion (blue points), respectively.
879 The straight lines are the trendlines of the linear regression between soil and C erosion.

880
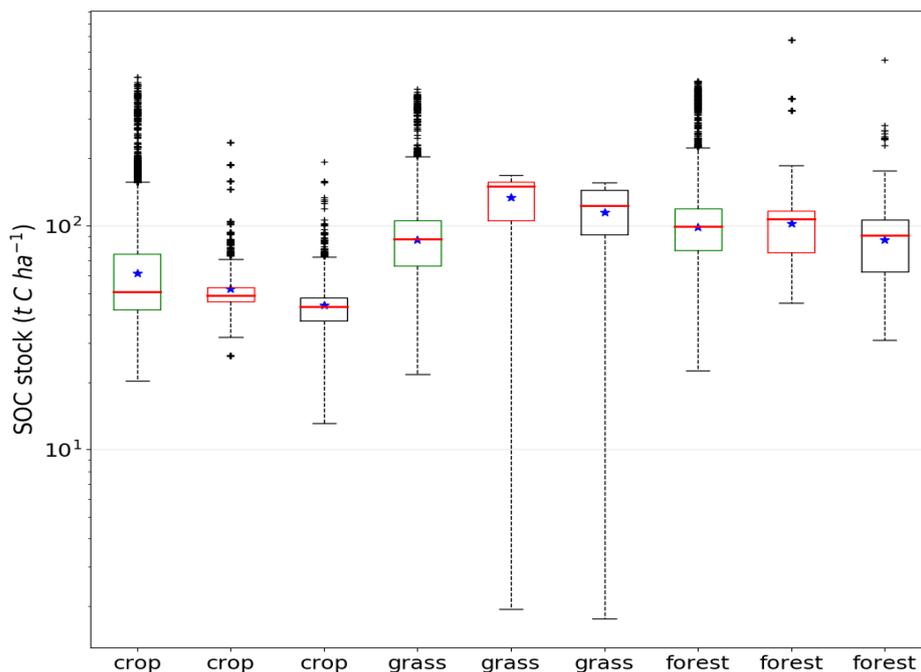
Figure 7: Comparison of total SOC stocks per land cover type between the simulation without erosion (red boxes), the simulation with erosion (black boxes) and the LUCAS data (green boxes). The red horizontal lines are the medians, the blue stars are the means, the dashed vertical lines represent the range between the minimum and maximum, and the black dots are the outliers.
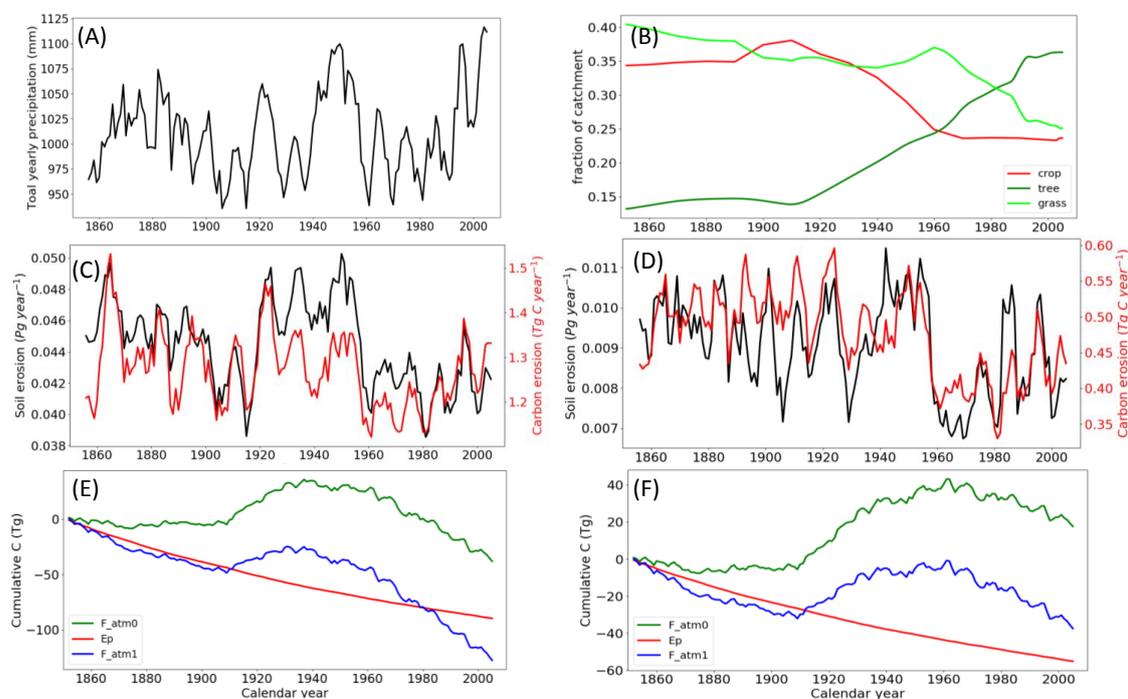
Figure 8: Timeseries of (A) the 5-year average yearly precipitation of the entire Rhine catchment (mm), (B) changing land cover fractions of the entire Rhine catchment, (C): 5-year average of the total gross soil erosion (Pg year^{-1}) and C erosion rates (Tg C year^{-1}) of the **entire Rhine** catchment, (D): 5-year average of the total gross soil erosion (Pg year^{-1}) and C erosion rates (Tg C year^{-1}) of the **non-Alpine region** of the Rhine. Erosion on bare soil is not taken into account here. (E) Cumulative C emissions from the soil to the atmosphere under land use change and climate change without soil erosion (F_atm0), with soil erosion (F_atm1), due to additional respiration or stabilization of buried soil and photosynthetic replacement of C under erosion (Ep) of the **entire Rhine** catchment. (F) Cumulative C emissions from the soil for the **non-Alpine part** of the Rhine catchment. Positive values indicate net C emissions to the atmosphere and negative values indicate net C uptake from the atmosphere by the soil.

902

903

904

(A)

NEP_{HS}
0.52

NEP_{FL}
0.53

905

906

907

E_{rep}
0.69

Rc_{net}
0.25

Ra_{net}
0.52

908

909

910

dSOC
1.05

POC$_{exp}$
0.0016

911

Ce
1.04

Dc
0.39

Da
0.65

912

913

dSOC$_{HS}$
-0.13

dSOC$_{FL}$
1.18

914

(B)

NEP_{HS}
1.66

NEP_{FL}
0.69

915

916

917

E_{rep}
0.96

Rc_{net}
0.365

Ra_{net}
0.21

918

919

920

dSOC
2.35

POC$_{exp}$
0.0026

921

Ce
1.02

Dc
0.376

Da
0.646

922

923

dSOC$_{HS}$
1.02

dSOC$_{FL}$
1.33

924

925
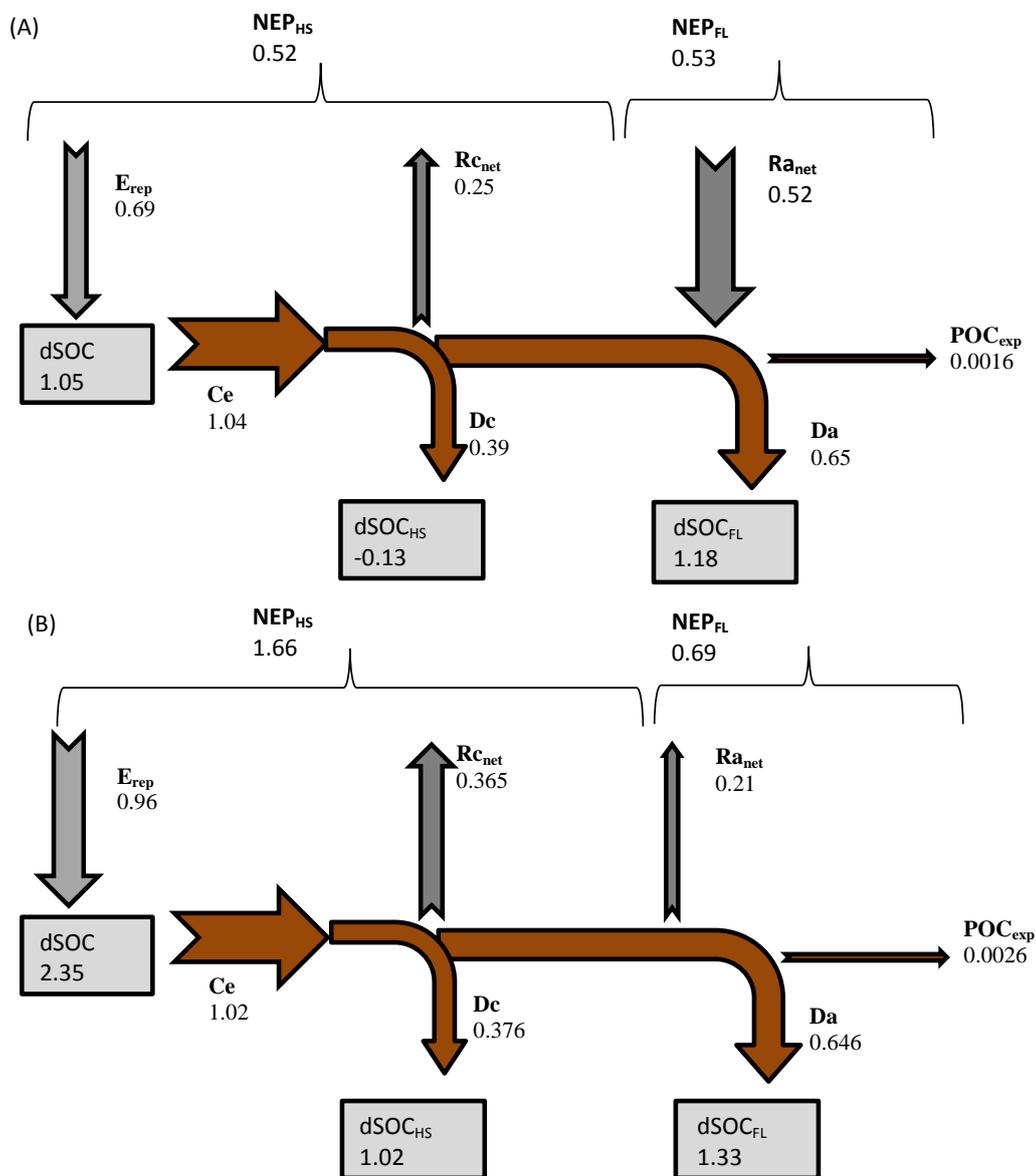
926 **Figure 9:** (A) C budget of the entire Rhine for the period 1851-1861, and (B) for the period 1995-2005. The budget shows

927 the net exchange of C (Tg C year^{-1}) between the soil and atmosphere as a result of accelerated soil erosion rates. Grey

928 arrows are the erosion-induced yearly average **vertical** C fluxes, while the brown arrows are the erosion-induced yearly

929   average **lateral** C fluxes. The grey boxes represent yearly average changes in SOC stocks for the specific time period as a

930   result of land use change, climate change, erosion and deposition. Dc: Deposition of C on hillslopes; Da: Deposition of C

931   in floodplains; POC_{exp}: net POC export flux; NEP_{HS}: Net ecosystem productivity of hillslopes; NEP_{FL}: Net ecosystem

932   productivity of floodplains; dSOC: Yearly average change in the total SOC stock; $dSOC_{HS}$: Yearly average change in the

933   hillslope SOC stock; $dSOC_{FL}$: Yearly average change in the floodplain SOC stock.

934
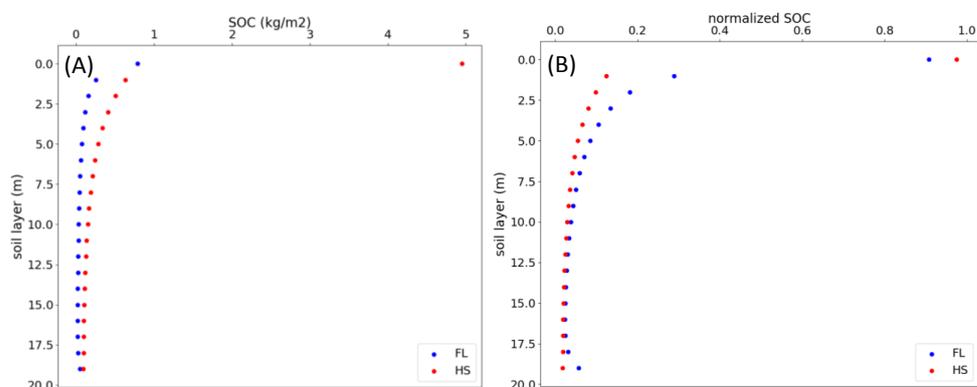
936 **Figure 10:** (A) Vertical distribution of hillslope (red) and floodplain (blue) SOC stocks (kg m^{-2}) with depth averaged over

937   the whole Rhine catchment, and (B) the vertical distribution of normalized hillslope (red) and floodplain (blue) SOC stocks

938   (dimensionless) with depth averaged over the whole Rhine catchment.